A Study of Low Cycle Fatigue Life and its correlation with Microstructural Parameters in IN713C Nickel Based Superalloy

J. Salvat Cantó, S. Winwood, K. Rhodes, S. Birosca

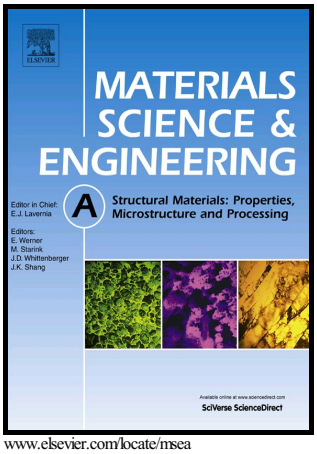

www.elsevier.com/locate/msea

PII: S0921-5093(18)30114-X
DOI: https://doi.org/10.1016/j.msea.2018.01.083
Reference: MSA36037

To appear in: *Materials Science & Engineering A*

Received date: 27 November 2017
Revised date: 19 January 2018
Accepted date: 22 January 2018

Cite this article as: J. Salvat Cantó, S. Winwood, K. Rhodes and S. Birosca, A Study of Low Cycle Fatigue Life and its correlation with Microstructural Parameters in IN713C Nickel Based Superalloy, *Materials Science & Engineering A,* https://doi.org/10.1016/j.msea.2018.01.083

A Study of Low Cycle Fatigue Life and its correlation with Microstructural Parameters in IN713C Nickel Based Superalloy

J. Salvat Cantó[1], S. Winwood[2], K. Rhodes[2], S. Birosca[1]

[1]Materials Research Centre, College of Engineering, Swansea University, Bay Campus, Swansea SA1 8EN, UK.

[2]Cummins Turbo Technologies, St. Andrews Rd., Huddersfield HD1 6RA, UK.

[*]Corresponding author. Address: Swansea University, Bay Campus, Fabian Way, Crymlyn Burrows, Swansea, SA1 8EN, UK. 840409@swansea.ac.uk

Abstract

Up to date, IN713C Nickel-based superalloy has been continued to be the best alloy candidate for turbocharger wheel applications due to its adequate fatigue property and resistance to degradation under harsh operating environments. Throughout this study, three different batches of as-cast IN713C nickel based superalloys with different microstructures including columnar, equiaxed and transition microstructures were investigated. Strain control Low Cycle fatigue (LCF) tests were conducted for the three different microstructures, achieving fatigue life between 100 and runout at 100,000 cycles, depending on the testing parameters. The fracture mechanics and failure mechanism were correlated to the alloy's microstructure, texture and chemical composition under various LCF conditions using optical microscopy, SEM, EDX and EBSD. In the current study an exact correlation between alloy's microstructure/microtexture and LCF endurance is established. The results showed that equiaxed microstructure has a superior fatigue life than the transition microstructure by 10% and columnar microstructure by > 200% at a given

temperature and strain rate. This large discrepancy was mainly due to the grain size differences between the studied microstructures. Here, it was evidenced that the grain size controls the dendrites length. It is also demonstrated that all microstructures exhibited a longer fatigue life at room temperature than at 650°C, doubling or tripling the fatigue life of the tested IN713C. Furthermore, the high presence of precipitates between dendritic arms in all three microstructures was found to have great influence on crack propagation path. It was apparent that segregated carbides in between dendritic arms caused secondary crack initiation and crack path undulations during the LCF tests.

Graphical abstract

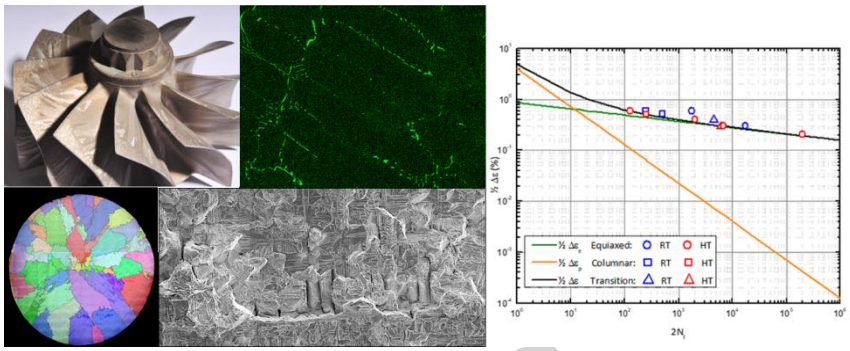

Keywords: Fatigue; IN713C; microstructure; investment casting; superalloy

1. Introduction

IN713C nickel-based superalloy have been widely used for turbocharger and jet engine applications due to their excellent mechanical properties and resistance to oxidation at elevated temperatures [1–8]. In commercial diesel engine, turbochargers are used as an effective technique for increasing the performance of the engines while reducing fuel consumption together with CO_2 and other pollutants emissions [1,9–13]. In general, turbine

wheels of commercial automobile turbochargers operates at a maximum temperatures of 750°C, with average operating temperatures around 650°C and a maximum rotation speed above 100,000 rpm [4,11,12,14,15]. In addition, the turbine wheel requires to be resistant to corrosion under harsh environments as it is constantly exposed to the exhaust gases from the engine. Furthermore, these turbine wheels have a complex geometry with different blade shape and curvatures. Hence, the investment casting has been the main manufacturing process of turbocharger wheels using the lost wax method. This method enables the manufacturing of complex component geometry at a relatively low cost and provides minimum material defects. However, due to the different cooling rates throughout the mould thickness the resultant microstructure may not be uniform and contain pores [3–5,8,13,16–18]. The typical microstructure of the turbine wheel generated via investment casting consists of large columnar grains along the blades, very fine equiaxed grains located at the blade tips with a transition region between the two regions. As any other nickel based superalloys, IN713C contains approximately 60-70% of the γ' ordered intermetallic hardening precipitate $L1_2$ Ni_3(Al, Ti, Ta, Nb) phase, γ matrix A1-Ni phase and carbides. The alloy can also contains topologically close-packed (TCP) phases, especially when exposed to long periods to high temperature environments. The TCP phases have different crystal structures than the matrix and more complex morphology, like tessellated layers of arrays stacked into a polyhedral coordination, *i.e.*, hexagons, pentagons or triangles, with a high and uniform packing density of atoms. They are also detrimental because of the strengthening elements depletion from the γ phase, such as Mo and Cr, becoming a probable crack initiation site during cyclic loading [4,6–8,13,17–23].

In most applications turbochargers are not constantly operating at the same speed, as the power required by the engine may not be constant during operation time. Thus, to consider the start-up conditions including loading cycles is vital, which is attributed to the centrifugal forces in the low frequency ranges. Thus, it is critical to prevent an early failure of turbocharger components under fatigue condition. This has greatly attracted both academia and industrial research activities to study the low cycle fatigue (LCF) behaviour and the effect of different microstructures on the crack initiation and propagation for the past 40 years [4,20,24]. However, the exact microstructure/property relationship and particularly the effect of the microstructure on crack initiation and growth still disputed in the literature. In the current study the exact influence of microstructure parameters such as grain size, orientation, morphology as well as dendritic structures on LCF crack initiation, growth, diversion and undulations is investigated.

2. Materials and experimental procedures

As reported in Section 1, and shown in Figure 1a-c, the microstructure of IN713C alloy following investment casting is not homogenous, which consists of large columnar grains, very fine equiaxed grains located at the blade tips with a transition region between the two. Figure 1c shows an EBSD orientation map for the blade tip area indicated by a dashed red rectangular area on the Figure 1a. As shown in Figure 1c, the grain sizes were in the range of 0.02 mm^2, 0.25 mm^2 and 9.10 mm^2 in the blade tip, transition and columnar areas, respectively. Moreover, due to complex geometry of the wheels, different thickness across the blades and bending issues it is rather impractical to extract a testing specimen from produced turbine wheel via investment casting, see Figure 1a,b. In order to study local

microstructure and texture correlation with mechanical properties, small punch testing discs were extracted from the transition zone by Coleman, *et al*., [25]. However, it was not possible to extract a small size specimen from equiaxed area due to small size of the region and bending issue, see Figure 1b. In the current study, in order to study the effect of different microstructures on the crack initiation and propagation, bars with different microstructure, *i.e*., equiaxed, columnar and transition, were produced individually via investment casting route. This allows to extract large specimens that can be used for standard low cycle fatigue testing. The geometry of the tested specimen is shown in the Figure 1d. Figure 2 shows the three different batches of as cast IN713C cylindrical bars that were supplied by Cummins Turbo Technologies Ltd, Huddersfield, UK, with the chemical composition shown in Table 1.

Table 1. Chemical composition of the IN713C alloy (wt%).

Element	**Ni**	**Cr**	**Al**	**Mo**	**Nb**	**Ti**	**Ta**	**Si**
wt%	71.1	13.4	6.4	4.8	2.9	0.7	0.4	0.3

The three batches consist of bars with fully equiaxed, fully columnar and transition microstructures, see Figure 2d-f. In order to obtain these different microstructures, each batch was produced from a separate casting tree with different mould coatings that can promote a specific grain size and shapes through the promotion of different nucleation points, see schematic in Figure 2a-c. Each batch consisted of several as cast cylindrical bars of 24 mm diameter and 100 mm length with the testing specimens being machined from the centre of the bars, see Figure 2d-f. It is evident that the exact size of actual equiaxed and columnar grains in real turbine wheel, see Figure 1, was not able to be reproduced through this method, see Figure 2, due to different geometry and component size between turbine

wheel and produced bars via investment casting. For instance, the average grain size for equiaxed, transition and columnar grain in actual turbine blades produced via investment casting are 0.02, 0.25 and 9.10 mm^2, respectively, see Figure 1a-c. Whilst the equiaxed, transition and columnar average grain sizes in the produced bars using coating technique were ~ 5.88 mm^2, 7.83 mm^2 and 21.58 mm^2, respectively. However, this grain size differences did not affect this specific simulation study for the crack initiation and propagation mechanism greatly as the main aim was to investigate the grain boundary characteristics and dendritic structure influence on the crack path rather than the grain size, which was produced via the same method.

The geometry of the fatigue specimens is shown in Figure 1c, with a gauge length of 12 mm and a gauge diameter of 4.5 mm. A total of eleven samples were subjected at low cycle fatigue testing under strain control. The tests were performed with an R ratio of -1 and a maximum strain ranging from 0.2% to 0.6%. The fatigue tests were conducted at room temperature and at 650 °C, which is close to the average operating temperature of a turbocharger turbine wheel. The strain control LCF test enables continuous direct measurement of the strain to observe non-homogeneous strain distribution effect during cycling loading test. On the other hand, the information acquired from stress control tests mainly belongs to elastic and unconstrained deformation. For many applications, the real components, including turbine wheels, generally undergo a certain degree of structural constraint and localised plastic flow, especially at locations of stress concentrations. These local stress concentrations leads to a significant fatigue life reduction, which is why the strain control LCF test was implemented in this investigation. Furthermore, two tensile tests

were carried for yield point determination. These tensile tests were carried out at room temperature and at 650 °C, to have an approximation of the yield stress and Young modulus, among other mechanical properties, at the two temperatures of interest.

Following the completion of strain control LCF tests, fracture surface study and microstructure characterisation were performed by means of optical microscopy (OM) and Scanning Electron Microscope (SEM, Zeiss EVO LS25). The samples were then sectioned and, to aid in metallographic analysis, mounted in conductive Bakelite prior to a series of grinding and polishing steps culminating in a final polish using a non-crystallising colloidal silica solution (0.04 μm) for 15 to 60 minutes. An etching process with Kalling's No. 2 was carried out to reveal the microstructure prior to further analysis using high resolution Field Emission Gun SEM (JEOL 7800F FEG SEM), Energy Dispersive X-ray Spectroscopy (EDS) and Electron Backscatter Diffraction (EBSD) analysis in order to investigate the exact correlation between crack path, diversion and undulation with the microstructure of the alloy. The EBSD data were collected using a Nordlys EBSD detector, AZTEC data acquisition software and the analysis was conducted using standard HKL Channel 5 software package.

3. Results and discussion

3.1. Mechanical characterisations

Figure 3 shows engineering Stress-Strain curves for IN713C nickel base superalloy with columnar microstructure tested at RT and 650 °C. From the figure, the yield strength and ultimate tensile strength values obtained during this investigation were very similar with the

values reported in literature for IN713C alloy [25,26]. Although temperature seems to have no significant effect on the yield strength, the ultimate tensile strength at high temperature was much higher than that at room temperature by ~ 90 MPa. High UTS at high temperature is expected due to increased ductility and the ease of dislocations movement at high temperature, however, the large difference found in this study might be also a consequence of a combined effect of the small gauge diameter, the large grain size and the microstructure heterogeneity of the alloy under these casting conditions. The disparity in the Young modulus values as shown in the same figure is also an indication of non-homogeneous microstructure generated during the bars' investment casting. The Young modulus values for each microstructure shown in Figure 3 were obtained from straining the specimens up to 0.2% strain at 650 °C. These Young modulus values and the ones shown in Table 2 from the LCF testing indicate the microstructure influence on the mechanical property of the alloy. This is a vital aspect in better understanding the local microstructure effects on deformation mechanism where non-homogeneous microstructure can exist across the turbine wheel. Further investigation of microstructure heterogeneity of the bars is performed on the fracture surface following the sample failure as discussed later in Section 3.2.

Table 2 shows the summary of the LCF testing conditions, cycles to failure, stress amplitude and young modulus for the specimens carried out throughout this study. The specimen notation used here was based on the sample microstructure (1st letter), test temperature (2nd and 3rd letters) and maximum strain (the las 2 two digits), see sample notation in the same Table. It is evident from the stress amplitude of the fatigue tests (see Table 2) and the

resultant yield strength of the tensile tests (see Figure 3) that the specimens tested at a maximum strains of 0.4% or lower were below the yield, so less plasticity was expected during LCF test. This particular testing condition used here can justify the increase of the alloy fatigue life with an order of magnitude between the specimens tested at 0.5% and 0.6% maximum strain and the ones at 0.3% and 0.4%. Furthermore, the only specimen that achieved the 100,000 cycle runout was the sole specimen tested at the lowest strain rate of 0.2%.

Table 2. Summary of the fatigue testing conditions and results.

Sample	Microstructure	T (°C)	ε_{max} (%)	Cycles to failure	σ_a (MPa)	E (GPa)
CRT06	Columnar	20	0.6	125	905	217
ERT06	Equiaxed	20	0.6	885	816	188
EHT06	Equiaxed	650	0.6	63	834	172
CRT05	Columnar	20	0.5	255	822	196
CHT05	Columnar	650	0.5	128	794	183
TRT04	Transition	20	0.4	2264	731	194
EHT04	Equiaxed	650	0.4	1005	673	179
ERT03	Equiaxed	20	0.3	8663	656	221
EHT03	Equiaxed	650	0.3	3376	478	171
THT03	Transition	650	0.3	3015	523	176
EHT02	Equiaxed	650	0.2	Run out (100,000)	346	170

Figure 4a show the strain amplitude-fatigue life for IN713C nickel base superalloy, with the superposition of the plastic and elastic strain amplitude-fatigue life model representations. As can be seen in Figure 4a, both elastic and plastic parts are observed from the strain amplitude-life curve, represented by the green and orange curves, respectively. Whilst the black curve represents the total strain, *i.e.* the sum of both the elastic and plastic strain

components. As shown in the figure, the major contribution to the strain come from the elastic component, with all the data points being very close to the elastic strain curve (green), even though for a LCF test high plastic strains were to be expected. As a consequence of this strain distribution, the transition life ($(2N_f)_t$) for this material is very low, meaning that the fatigue life is expected to be dictated by the rupture strength rather than ductility. From Figure 4a it can also be seen that the equiaxed microstructure showed higher fatigue life than the transition or columnar microstructures at a given strain and temperature. These observations can be seen more clearly in Figure 4b, where the effect of microstructure on the cycle to failure of the IN713C alloy is shown. It is evident from the figure that, at a given strain level and temperature, equiaxed microstructure has a higher fatigue life than the columnar or transition microstructures. It is also clear from the same figure that IN713C alloy always showed lower resistance to fatigue at HT (650 °C) than at RT.

The obtained strain controlled fatigue data for all the produced microstructure at HT and RT were plotted to fit the existing fatigue life models including Basquin and Coffin-Manson models [27,28]. Figure 4c shows the plastic strain amplitude versus the fatigue life data with the Coffin-Manson model calculation at each temperature. The Coffin-Manson model is generally based on the plastic strain amplitude. Although Figure 4a showed that the elastic strain was more significant than the plastic one, however, this model is considered as a standard model for strain-based approach to total fatigue life for smooth-surfaced components [27,28]. The plastic strain-reversals to failure relationship is as follows:

$$\frac{\Delta\varepsilon_p}{2} = \varepsilon_f'\left(2N_f\right)^c \quad (1)$$

where $\Delta\varepsilon_p/2$ is the plastic strain amplitude, $2N_f$ the number of reversals to failure, ε_f' is the fatigue ductility coefficient and c is the fatigue ductility exponent. As can be seen in Figure 4c, the curve fitting for the data obtained at high temperature had a relatively better fit, compared to the data obtained at room temperature which had a wide spread to interpolate the Coffin-Manson model. Furthermore, the stress amplitude versus the fatigue life data obtained for all the microstructure were fitted with the elastic Basquin model, as shown in Figure 4d, using equation 2:

$$\frac{\Delta\sigma}{2} = \sigma_a = \sigma_f'\left(2N_f\right)^b \qquad (2)$$

where σ_a is the stress amplitude, $2N_f$ the reversals to failure, σ_f' is the fatigue strength coefficient and b is the fatigue strength exponent. As shown in Figure 4d and Table 3 the Basquin model fits accurately for both high and room temperatures. The curve fitting method used in the current study was based on the coefficient of determination (R^2), which is a statistical measure of how close the data are to the fitted regression line, and, since a high R^2 value does not necessary imply a better fit, the tolerance obtained for each fitting had been taken into account too. As shown in Table 3, the R^2 value for the Coffin-Manson is very low for the fitting at RT, with a very high tolerance values for both the fatigue ductility coefficient and exponent, supporting the observation from Figure 4c and the RT data large spread to fit the Coffin-Manson model. Moreover, the HT data showed better fitting, with a good R^2 value, as it can be seen from Table 3, but the tolerance for the fatigue ductility coefficient is too high, *i.e.*, ~ half the value of the coefficient, meaning that is not a good fitting either. Furthermore, the Basquin fittings for both the RT and HT data have good R^2 values, see Table 3. The tolerance for the fatigue strength coefficient and exponent are acceptable for both tested temperatures which are below 15% of the value in the worst

case. From the analysis of both factors, R^2 and tolerance, it is safe to claim that the data fits well into the Basquin model for both temperatures.

Table 3. Cyclic strain-life parameters obtained for the Coffin-Manson and Basquin models calculations with their coefficient of determination, both for room temperature and 650 °C.

Temperature	**Coffin-Manson**			**Basquin**		
	ε_f' (%)	**c**	**R^2**	**σ_f' (MPa)**	**b**	**R^2**
RT	1.6±2	-0.4±0.2	0.491	1317±103	-0.07±0.01	0.915
650 °C	4.2±2	-0.75±0.08	0.988	1550±146	-0.12±0.01	0.953

Combining the Coffin-Manson (1) and Basquin (2) equations and noting that

$$\frac{\Delta\varepsilon}{2} = \frac{\Delta\varepsilon_e}{2} + \frac{\Delta\varepsilon_p}{2} \quad (3)$$

$$\frac{\Delta\varepsilon_e}{2} = \frac{\Delta\sigma}{2E} = \frac{\sigma_a}{E} \quad (4)$$

where E is the Young's modulus, an equation for the total life can be obtained:

$$\frac{\Delta\varepsilon}{2} = \frac{\sigma_f'}{E}(2N_f)^b + \varepsilon_f'(2N_f)^c \quad (5)$$

which has been used to represent the total life in Figure 4 (a). It should be noted that the orange line in the same figure, which represents the plastic strain, is obtained from the equation 1, and the green line, representing the elastic strain, from the first term on the right hand side of equation 5. Thus comparing and plotting the fatigue life data with both model curves as shown in Figure 4a, two prominent observations arise:

- The obtained LCF data validates the total fatigue life prediction model using Equation 5 (see the black line in Figure 4a).

- The transition life ($(2N_f)_t$), which separates the plastic strain dominant region from the elastic strain dominant region, is very low, *i.e.*, ~ ten reversals. This indicates that the fatigue life is dictated more by rupture strength than ductility [27] and led to better fitting of the strain control fatigue data with the Basquin model, than the Coffin-Manson model.

Moreover, the fatigue life data was best fitted with Basquin model at both high and room temperatures, while Coffin-Manson model can only relatively fit the data obtained at high temperatures. This may be due to the slightly enhanced plasticity of the material at the high temperatures and increasing the possibility of further slip system activation. It is clear that at high temperature the fatigue life is partially influenced by the ductility of IN713C alloy, hence the better fitting for the fatigue life data at HT than at RT for the Coffin-Manson model, as this model based on plasticity. It also appears that the increased ductility at high temperature led to a shorter fatigue life than at RT, see Figure 4a-d and Table 2. As shown in Figure 4b, for a given strain rate, IN713C alloy has a better fatigue life at room temperature than at high temperature, independent of the microstructure. Furthermore, it is clear from the same figure that, at a given strain rate and temperature, equiaxed microstructure has a longer fatigue life than columnar or transition microstructures and this aspects will be discussed in Section 3.2.

3.2. Microstructure and microtexture correlation with LCF failure mechanism

3.2.1 Microstructure characterisation of the original as-cast alloy

As shown in Figure 5, the produced as cast bars with equiaxed, columnar and transition microstructures discs were cut in several locations in order to observe the microstructure

changes along the bar casting direction. However, here the micrographs show only 2 main locations, *i.e.*, bottom and centre of the bars, where most microstructural alteration should occur. It should be noted that a critical change in the transition microstructure should be observed at the centre of the produced bar, where the significant cooling rate changes occurred, see Figure 2b and 2e. The grain size at the bottom and centre discs in the transition cast bar were 8.82 mm^2 and 6.84 mm^2, respectively. As can be seen in Figure 5b, the grain size for equiaxed grains was smaller, being 5.85 mm^2 and 6.68 mm^2 in bottom and centre discs respectively, whereas the grains size for the columnar bar were 25.92 mm^2 at the bottom disc, and 17.24 mm^2 in the centre disc. Although the equiaxed microstructures were obtained via bar casting techniques showed in Figure 2, however, the produced equiaxed grain size was much larger than what it is in the actual turbocharger wheels at least by 250 times, compared to the grain size in the turbocharger wheels stated in Section 2. For the transition microstructure, the grain size obtained was also larger than in the actual component, by nearly 50 times. Finally, for the columnar microstructure, although the grain size has been tripled, the difference between real component and testing material was smaller than other two microstructures. The main reason for this increase in grain size was due to the size and geometry of the cast component that greatly affected the cooling rate. Although there are differences in grain size between the actual component and the testing material for each microstructure, this discrepancy was not critical for this study as the aim here was to produce 3 different microstructure and investigate the effect of microstructural features on fatigue life as well as crack initiation and propagation.

EBSD maps of the discs for all three different microstructures are shown in Figure 6. The figure shows Inverse Pole Figure (IPF) maps parallel to the casting direction, *i.e.* Z axis, for each microstructure. It should be noted that the casting direction is also the loading direction used during the LCF tests. It is evident from the figure that the grains were randomly oriented and no predominant specific texture component was generated in any of the three microstructures during bar casting. This is more evident in the equiaxed microstructure, see Figure 6a, due to the smaller grain size and, therefore, higher number of grains. For example, in the transition sample, Figure 6b, there were some pairs of big grains with textures close to Cube (red) or Copper (blue), but in both cases being more than 15° away from the ideal orientation and overall produced random orientation distribution. Although there are clear differences in grain size and shape between all three microstructures, however, as shown in Figure 7, they all contain visible dendritic microstructure. The dendrites structure that are generated during the solidification process have a different direction and length within each grain, depending on the grain orientation, see Figure 7b. It is clear from the figure that some of the primary arms have lengths of several millimetres. As it will be further discussed in the Section 3.2.2, these dendrites play an important role in the crack propagation and secondary crack initiation processes. Therefore, as the grain size determines the length of these dendrites, it is also an important parameter for the fatigue life study. Furthermore, the element segregation along the interdendritic and dendritic regions will be also discussed in the next section, as well as the effects of this segregation on the mechanical and fatigue properties of IN713C nickel based superalloy.

3.2.2 Fracture surface study of the failed IN713C alloys

Fractographic analysis was conducted on the failed LCF tested specimens following ultrasonic cleaning of the surface in acetone solution. Figure 8 shows the fracture surface of two specimens with equiaxed microstructure failed at room temperature; ERT06 in (a) and at 650 °C; EHT04 in (b). The distinct difference between the two fracture surfaces is the oxidation present at high temperature and in particular in the crack initiation and microstructural propagated area as indicated in Figure 8b. In general, the fracture surface for both samples were flat and contain one or two crack initiation sites. However, in case of multi crack formation there was ~ 1 mm height difference along the loading direction between the two crack initiation sites. Increasing the stress level during the LCF test, one of the crack retarded (see the yellow dashed ellipse in Figure 8b) due to crack shielding mechanism and the major crack advanced until the sample failure. Furthermore, the presence of large dendrites can be clearly seen in both specimens, see the dashed red lines on Figure 8a, b and d, showing the major dendritic arm length and directions. However, the dendritic areas were more noticeable in EHT04 than in ERT06, see the top blue area in Figure 8b, where the dendritic areas were preferentially oxidised during the LCF test at high temperature. The high magnified images of dendritic structure on the fracture surface of a columnar specimen, CHT05, are shown in Figure 8c and 8d. It is interesting to see the apparent dendritic structure on the fracture surface which is indicative of the significant influence of the dendrites on the fracture mechanics and deformation mechanism. This also indicates on the non-coherent interface between the dendritic and interdendritic areas, see some selected areas in Figure 8c, and dendritic arm directions in Figures 8b and 8d along the crack direction. As shown in Figure 8b and indicated by yellow dashed ellipse, two distinctive areas can be observed. These two regions indicate the extent of the Stage II, which is the non-crystallographic crack growth and propagation, usually displaying a

smoother surface than Stage III, or final mechanical fracture [29,30]. When comparing the fracture surface of other specimens, a correlation with an inverse proportionality between the maximum strain applied and this extent of the Stage II was found.

Figure 9a-c show the SEM observation of the fracture surface of ERT06, CRT06 and EHT04 samples respectively. It is clear from the figure that dendritic arm lines as well as their intersection are very visible across the microstructurally crack propagated areas and mechanically failed areas in all three samples. Looking at high magnification of the fracture surface as in Figure 9d-e, the intersections of the primary and secondary dendritic arms created evident square shapes and parallel lines. Furthermore, it is clear from Figure 9d that secondary cracks and voids, as pointed by red arrows, were easily formed along the dendrite boundaries and provided a connected path for the primary and secondary crack propagation. It seems that most of the square shapes on the fracture surface as observed here were a product of the growth competition of the secondary dendrite arms, as shown in Figure 9. Alloying element segregation during solidification, which is widely reported in literature [2,4,22,23,25,31,32], is expected to reside on the square pattern lines and intersections which in turn further highlight the square shapes on the fracture surface, as discussed thoroughly in the next section.

Due to relatively large grain size in all three microstructures studied here, no significant differences of fracture surface observation were found here. The larger grain size provided long primary dendritic arms and similar cubic structure, due to secondary arms interactions, all along fracture surface in all three microstructures. Thus, cross section investigation by

mean EBSD, EDS and HR SEM was needed to underline failure mechanism difference between the various microstructures.

3.2.3 Dendrite and Carbide distributions effects on LCF crack propagation

Further study was conducted to investigate the crack initiation sites following LCF tests under various conditions. Thus, cross sections of the specimens were prepared for OM, SEM, EDS and EBSD investigations. All the failed specimens were etched with Kalling's reagent No. 2 to reveal the microstructural features. As shown in Figure 10, the major crack was initiated at the surface of the specimen in all three microstructures; see the red arrow on equiaxed (Figure 10a), transition (Figure 10b) and columnar (Figure 10c) samples. The microstructure differences between the specimens was apparent in the same figure. For instance, the equiaxed microstructure has the smallest grain size among the 3 samples with a grain size of ~5.3 mm^2, columnar has the bigger grains (~10.4 mm^2), while the transition microstructure grain size laid between the two (in the range of ~8.7 mm^2).

Table 4. Chemical composition (wt%) of the γ', dendritic and interdendritic areas shown in Figure 11.

Area	**Element (wt%)**						
	Ni	**Cr**	**Al**	**Nb**	**Mo**	**Zr**	**Ti**
Coarse γ'	77.0	5.2	8.5	4.3	2.0	1.7	1.4
Interdendritic	70.5	15.5	5.5	1.9	5.9	0.1	0.6
Dendritic	74.3	12.9	6.3	1.6	4.1	0.1	0.5
Segregation ratio	0.95	1.20	0.87	1.19	1.44	1.00	1.20

Figures 11a, 11b and 11c-i show the etched SE image, backscattered SEM image and EDS 2D maps, respectively. It is clear from the figures that significant alloying element partitioning occurred during solidification process. From the figure, it is evident that the γ' former Al is preferentially partitioned in the dendritic region whereas Cr, Mo, Nb and Ti are partitioned

in the interdendritic regions, as it can be seen also in Table 4 with the EDS point analysis from the interdendritic and dendritic areas. This evidence is also supported by the values of the segregation ratio shown in Table 4, with this segregation ratio being calculated from the following equation, adapted from the study of Bhambri *et al.* [33]:

$$Segregation\ ratio = {}^{C_i}/_{C_d} \quad (6)$$

In equation 6, C_i represents the interdendritic solute concentration and C_d the dendritic solute concentration. Therefore, the value of this segregation ratio indicate if an element is more prone to segregate at the interdendritic areas, with a ratio >1, or at the dendritic regions, with a ratio <1. This strong segregation phenomenon occurred during solidification process would lead to thermodynamically suitable condition for second phase precipitation, carbide, boride as well as TCP formation. Figure 12 shows further evidence of the element segregation between dendritic and interdendritic regions, with the SEM image of the dendrites in the area of interest in Figure 12a, the layered (sum of elements) EDS 2D map in Figure 12b and the individual element EDS 2D maps in Figure 12c-i. It is apparent from the figure that the element segregation is accentuated and highlighted along the parallel and intersecting secondary dendritic arms. Both figures 11 and 12 clearly show the carbide formation along the dendritic/interdendritic interface. The detailed chemical analysis showed that there is a segregation of carbide formers, *i.e.*, Cr or Mo, in interdendritic regions. Moreover, from the individual EDS spectra, see Table 4, there was a high concentration of Ti, Al (γ‘ formers), Nb and Zr, and a low concentration of Cr and Mo in coarse γ‘. It is well established that Cr and Mo are generally partitioned in γ-gamma matrix [4,25] and form non-coherent carbides. It is also evident from Figure 11 that the carbide were precipitated in an ordered fashion all along dendritic structure and building up stacks

of these patterns that can reach hundreds of microns in length. It is well reported in the literature [4,25,34] that carbides are a hard and brittle phase in addition to their non-coherent nature to the matrix. Hence the carbide can act as secondary crack initiation sites or easy crack propagation paths in solidified alloy, see Figure 9d. The carbide size differences between the three microstructures were negligible. All three microstructures showed mainly elongated carbides with lengths between 1 and 60 microns and widths between 0.1 and 8.5 microns. The average area was around 7 μm^2 for equiaxed and transition microstructures while for the columnar one it was around 8 μm^2, with the difference being smaller than the standard deviation of the measures. Finally, the carbide area fraction obtained was 1.6, 1.4 and 1.3%, for the equiaxed, columnar and transition microstructure, respectively, with a standard deviation of 0.2%.

From Figure 13 it is clear that the carbide segregation on the dendrite/interdendritic interfaces has a great influence of the crack propagation and deviation during LCF test. It is evident from the same figure that the crack propagated along the dendritic arms boundaries and followed the dendritic shape. It is also clear that the crack was propagating toward the hard carbides in order to reach the highly strained area due to incoherent interface between the carbide and matrix, where it acts as stress concentration factor within the microstructure, as shown in Figure 13b, which is the magnification of the area indicated in Figure 13a. This eventually led to linkage of the microcracks that generated and grown on the carbides to form a continuous propagated crack path along the dendritic arms. During the development of these continuous cracks, when the carbides have an elongated shape parallel to the loading direction, even the preferred crack growth direction is perpendicular

to the loading direction, due to the carbide brittleness, the cracks tend to grow in a serrated way, as shown in Figure 13b, combining the preferred perpendicular direction and the easy parallel direction along the carbides.

3.2.4 The influence of grain orientation on fatigue crack initiation

Figure 14 shows Electron Backscattered Diffraction (EBSD) maps of the three samples from Figure 10. Figure 14a-c show Inverse Pole Figures (IPF)s parallel to the loading as well as casting (Y) direction, for equiaxed, transition and columnar microstructure in (a), (b) and (c) respectively. From all the LCF tested specimens investigated here, in 40% of the specimens the crack initiated on a Cube ({001} <100>) or Goss ({110} <001>) oriented grains, and 20% on a Copper ({112} <111>) oriented grain. While the failure in the rest of the specimens were found to be independent of grain orientation or any specific texture components. From these results, it was apparent that texture can influences the crack initiation, and promote fracture within the grains that close to <100>-fibre texture. This fibre happens to have the same direction than the fast-growing dendritic orientation for nickel-base superalloys [35]. It should be noted here, that the loading direction used in the LCF test is parallel to casting direction during solidification process. This clearly indicates that the primary dendritic arms growth direction is parallel to the <100> direction and, as the secondary dendritic arms are perpendicular to the primary arm direction, their growth direction is again <100> from a crystallographic point of view. As the intersection between <100> directions is 90°, thus, this explain the square shape and cubic nature of the dendritic arm morphology observed on the fracture surface, see again Figure 9.

Furthermore, from the EBSD maps in Figure 14, the microstructure differences, such as the smaller grain size of the equiaxed and transition microstructures (Figures 14a and 14b, respectively) can be clearly seen compared with the columnar sample (Figure 14c).

Furthermore, it is clear from the {111}[110] slip system Schmid factor maps with the loading direction parallel to Y direction for equiaxed, transition and columnar microstructure in Figure 14d, 14e and 14f respectively, the Cube and Goss oriented grain have highest Schmid factor (0.46, 0.47 and 0.46 respectively) where the crack initiated. Moreover, the other grains with even higher Schmid factor in the map did not contribute in the crack initiation or propagation due to their location in the centre of the specimen. As stated by Gelmedin and Lang [24], for LCF tests on IN713C, cracks usually initiate below the surface when there is a concentration of defects, such as pores, and since no pores were detected in the studied specimens, the crack was to be expected to initiate at the surface, even if the grains with higher Schmid Factor were subsurface. Moreover, when a surface grain without a <100>-fibre texture component had a higher Schmid factor than a nearby Cube or Goss texture component grains, as shown in Figure 14e, the crack still initiated at the <100>-fibre grain, supporting the claim of the influence of the grain texture for crack initiation.

In summary, although there were differences in grain size between the real turbine wheel and the experimental cast material, yet the equiaxed microstructure had a smaller grain size than transition microstructure, which also had a smaller grain size than the columnar microstructure. Thus the grain size correspondence of the actual wheel microstructures was retained in the cast trials, see Figures 1c, 5b and 6a-c. All microstructures had a high

presence of dendritic structures, as shown in Figures 7-9, 11 and 12, due to solidification process, leading to element segregation along the dendritic and interdendritic regions, with carbides being mainly trapped in the interdendritic areas, see Figures 11-12 and Table 4. This concentration of carbides along the dendrite arms enhanced the initiation and propagation of secondary cracks following the dendritic arm directions, as shown in Figure 9d. At a given strain rate, all the three microstructures showed a longer fatigue life at RT than at HT (Figure 4a-b and Table 2) due to increased ductility at 650°C. Whilst, at a given strain rate and temperature the equiaxed microstructure had longer fatigue life than the transition and columnar microstructures. This is due to smaller grain size for the equiaxed microstructure, leading to less areas with a continuous dendrite arms in the same direction and more grain boundaries to act as obstacle for crack propagation and enhance fatigue crack propagation resistance in IN713C alloy. Finally, all the failed specimens had the crack initiated at the surface, predominantly in a grain with an orientation along the <100>-fibre texture, such as Cube or Goss texture components, which coincides with the fast-growing dendritic direction for nickel-based superalloys. In the current study the main microstructural parameters determining the low cycle fatigue life were found to be grain size and the orientation of the surface grains in the absence of porosity.

4. Conclusions

The performance of three different microstructures of IN713C have been investigated at room and high temperature under strain control LCF conditions. The main conclusions are:

- For all three microstructures, a better fatigue life is achieved at room temperature than at high temperature at a given strain rate, being 2-3 times longer at 20°C than

at 650°C, *e.g.*, 8663 and 3015 cycles for equiaxed samples tested at 0.3% maximum strain at room temperature and high temperature, respectively. This is related to the ease of slip activation at high temperatures and increased ductility.

- Equiaxed microstructure has a longer fatigue life than the other microstructures at a given temperature and strain rate. While equiaxed microstructure has only a slightly longer life than the transition one, by only 1.3 times. However, the fatigue life of equiaxed microstructure was much longer than that for columnar microstructure, by 2 to 7 times, with this difference being bigger at higher strain rates. The grain size and shape has an important role in fatigue crack propagation. The grains in columnar microstructure tend to be bigger, 22 mm^2 on average, and elongated along the loading direction, which further facilitate the crack propagation. Although transition microstructure also showed elongated grains along the loading direction, their size is much smaller than for the columnar, with an average of 8 mm^2, while equiaxed microstructure tend to have the smaller grains, with an average of 6 mm^2. Furthermore, the higher presence of grain boundaries and different dendrite orientations in equiaxed microstructure contributed to the longer fatigue life than in samples of other microstructures.
- High presence of lengthy primary dendrite arms with secondary arms competing for growth creating square structures. Precipitates, mainly carbides are trapped in between the dendritic arms due to alloying element segregation during solidification. Although the carbide area fraction is between 1.3 and 1.6%, carbide presence was mainly along the dendritic arms. The carbide precipitates are hard and brittle so that can fragment easily and provide easy crack paths as well as originate secondary cracks.

- The crack tends to initiate on the surface grains that have a <100>-fibre texture components, *i.e.*, Cube and Goss, which in turn is the preferential dendritic fast growth direction. This greatly facilitated an easy crack initiation in Cube and Goss oriented grain during LCF tests.

Acknowledgements

The authors would like to thank EPSRC for the financial support under EP/M506242/1 EPSRC DTP grant, Cummins Turbo Technologies for supplying the materials and the SEM facilities at Swansea University funded by EPSRC and the European Regional Development Fund through the Welsh Government.

References

[1] L. Kunz, P. Lukáš, R. Konečná, S. Fintová, Casting defects and high temperature fatigue life of in 713LC superalloy, Int. J. Fatigue. 41 (2012) 47–51. doi:10.1016/j.ijfatigue.2011.12.002.

[2] F. Zupanič, T. Bončina, a. Križman, F.D. Tichelaar, Structure of continuously cast Ni-based superalloy Inconel 713C, J. Alloys Compd. 329 (2001) 290–297. doi:10.1016/S0925-8388(01)01676-0.

[3] S. Pattnaik, D.B. Karunakar, P.K. Jha, Developments in investment casting process - A review, J. Mater. Process. Technol. 212 (2012) 2332–2348. doi:10.1016/j.jmatprotec.2012.06.003.

[4] R.C. Reed, The Superalloys - Fundamentals and Applications, Cambridge University Press, 2006.

[5] C.H. Konrad, M. Brunner, K. Kyrgyzbaev, R. Völkl, U. Glatzel, Determination of heat transfer coefficient and ceramic mold material parameters for alloy IN738LC investment castings, J. Mater. Process. Technol. 211 (2011) 181–186. doi:10.1016/j.jmatprotec.2010.08.031.

[6] F. Binczyk, J. Śleziona, A. Koscielna, Effect of modification and cooling rate on the microstructure of IN-713C alloy, Arch. Foundry Eng. 9 (2009) 5–9.

[7] A.C. Yeh, K.W. Lu, C.M. Kuo, H.Y. Bor, C.N. Wei, Effect of serrated grain boundaries on the creep property of Inconel 718 superalloy, Mater. Sci. Eng. A. 530 (2011) 525–529. doi:10.1016/j.msea.2011.10.014.

[8] H. Matysiak, M. Zagorska, A. Balkowiec, B. Adamczyk-Cieslak, R. Cygan, J. Cwajna, J. Nawrocki, K.J. Kurzydłowski, The microstructure degradation of the in 713C nickel-based superalloy after the stress rupture tests, J. Mater. Eng. Perform. 23 (2014) 3305–3313. doi:10.1007/s11665-014-1123-4.

[9] T. Hiroshi Uchida, Trend of Turbocharging Technologies, R&D Rev. Toyota CRDL. 41 (2006) 1–8.

[10] J. Galindo, J.R. Serrano, X. Margot, a. Tiseira, N. Schorn, H. Kindl, Potential of flow pre-whirl at the compressor inlet of automotive engine turbochargers to enlarge surge margin and overcome packaging limitations, Int. J. Heat Fluid Flow. 28 (2007) 374–387. doi:10.1016/j.ijheatfluidflow.2006.06.002.

[11] K. Jiao, H. Sun, X. Li, H. Wu, E. Krivitzky, T. Schram, L.M. Larosiliere, Numerical

simulation of air flow through turbocharger compressors with dual volute design, Appl. Energy. 86 (2009) 2494–2506. doi:10.1016/j.apenergy.2009.02.019.

[12] J. Filipczyk, Causes of automotive turbocharger faults, Transp. Probl. 8 (2013) 5–11.

[13] A. Sato, H. Harada, A.-C. Yeh, K. Kawagishi, T. Kobayashi, Y. Koizumi, T. Yokokawa, J.-X. Zhang, A 5th generation Sc superalloy with balanced high temperature properties and processability, Superalloys. (2008) 131–138.

[14] W.J. Chen, Rotordynamics and bearing design of turbochargers, Mech. Syst. Signal Process. 29 (2012) 77–89. doi:10.1016/j.ymssp.2011.07.025.

[15] B. Schweizer, M. Sievert, Nonlinear oscillations of automotive turbocharger turbines, J. Sound Vib. 321 (2009) 955–975. doi:10.1016/j.jsv.2008.10.013.

[16] P.K. Sung, D.R. Poirier, S.D. Felicelli, E.J. Poirier, A. Ahmed, Simulations of microporosity in IN718 equiaxed investment castings, J. Cryst. Growth. 226 (2001) 363–377.

[17] Z. Li, J. Xiong, Q. Xu, J. Li, B. Liu, Deformation and recrystallization of single crystal nickel-based superalloys during investment casting, J. Mater. Process. Technol. 217 (2015) 1–12. doi:10.1016/j.jmatprotec.2014.10.019.

[18] L. Liu, R. Zhang, L. Wang, S. Pang, B. Zhen, A new method of fine grained casting for nickle-base superalloys, J. Mater. Process. Technol. 77 (1998) 300–304. doi:10.1016/S0924-0136(97)00432-9.

[19] G. Xie, J. Zhang, L.H. Lou, Effect of cyclic recovery heat treatment on surface recrystallization of a directionally solidified superalloy, Prog. Nat. Sci. Mater. Int. 21 (2011) 491–495. doi:10.1016/S1002-0071(12)60088-4.

[20] T.M. Pollock, S. Tin, Nickel-Based Superalloys for Advanced Turbine Engines: Chemistry, Microstructure and Properties, J. Propuls. Power. 22 (2006) 361–374. doi:10.2514/1.18239.

[21] G.D. Pigrova, TCP-phases in nickel-base alloys with elevated chromium content, Met. Sci. Heat Treat. 47 (2005) 544–551. doi:10.1007/s11041-006-0029-7.

[22] C.M.F. Rae, R.C. Reed, The precipitation of topologically close-packed phases in rhenium-containing superalloys, Acta Mater. 49 (2001) 4113–4125. doi:10.1016/S1359-6454(01)00265-8.

[23] N. El-Bagoury, a. Nofal, Microstructure of an experimental Ni base superalloy under various casting conditions, Mater. Sci. Eng. A. 527 (2010) 7793–7800. doi:10.1016/j.msea.2010.08.050.

[24] D. Gelmedin, K.H. Lang, Fatigue behaviour of the superalloy in 713C under LCF-, HCF- and superimposed LCF/HCF-loading, Procedia Eng. 2 (2010) 1343–1352. doi:10.1016/j.proeng.2010.03.146.

[25] M.J. Donachie, S.J. Donachie, SUPERALLOYS Second Edition, Second Edi, ASM International, 2002.

[26] Engineering properties of Alloy 713C, Nickel Inst. (n.d.).

[27] S. Suresh, Fatigue of Materials, Cambridge University Press, 1998. doi:10.1017/CBO9780511806575.

[28] D. Lee, T. Kang, J.M. Koo, C.S. Seok, S.J. Song, A study of the LCF characteristics of the Ni-based superalloy IN738LC, Int. J. Precis. Eng. Manuf. 16 (2015) 775–780. doi:10.1007/s12541-015-0102-5.

[29] L. Kunz, P. Lukáš, R. Konečná, Initiation and propagation of fatigue cracks in cast IN713LC superalloy, Eng. Fract. Mech. 77 (2010) 2008–2015. doi:10.1016/j.engfracmech.2010.02.002.

[30] K.S. Chan, Roles of microstructure in fatigue crack initiation, Int. J. Fatigue. 32 (2010) 1428–1447. doi:10.1016/j.ijfatigue.2009.10.005.

[31] S. Zlá, B. Smetana, M. Žaludová, J. Dobrovská, V. Vodárek, K. Konečná, V. Matějka, H. Francová, Determination of thermophysical properties of high temperature alloy IN713LC by thermal analysis, J. Therm. Anal. Calorim. 110 (2012) 211–219. doi:10.1007/s10973-012-2304-8.

[32] Q. li Zhang, J. hua Yao, J. Mazumder, Laser Direct Metal Deposition Technology and Microstructure and Composition Segregation of Inconel 718 Superalloy, J. Iron Steel Res. Int. 18 (2011) 73–78. doi:10.1016/S1006-706X(11)60054-X.

[33] A.K. Bhambri, T.Z. Kattamis, J.E. Morral, Cast Microstructure of Inconel 713C anct its Dependence on Solidification Variables, Metall. Trans. B. 6B (1975) 523–537.

[34] N. Boutarek, D. Saïdi, M. a. Acheheb, M. Iggui, S. Bouterfaïa, Competition between three damaging mechanisms in the fractured surface of an Inconel 713 superalloy, Mater. Charact. 59 (2008) 951–956. doi:10.1016/j.matchar.2007.08.004.

[35] Y.Z. Zhou, A. Volek, N.R. Green, Mechanism of competitive grain growth in directional solidification of a nickel-base superalloy, Acta Mater. 56 (2008) 2631–2637. doi:10.1016/j.actamat.2008.02.022.

Figure Captions:

Figure 1: Photographs of a turbocharger turbine wheel showing the complex geometry of the blades and how the microstructure evolves through the blades (a and b). EBSD orientation map of the area indicated by a red dashed square in (a) showing the distribution of equiaxed, transition and columnar grains along the blade tip (c). Geometry of the fatigue specimens used in this study, all dimensions in mm (d).

Figure 2: Schematic of the different casting shells used to produce the three different microstructures: equiaxed (a); transition (b); and columnar (c). Resultant bars for each batch: equiaxed (d); transition (e); and columnar (f).

Figure 3: Engineering stress-strain curves for IN713C superalloy with columnar microstructure tested at RT and HT with the mechanical properties obtained. Table with Young's Modulus values for specimens of each microstructure tested at high temperature.

Figure 4: a) The total strain amplitude versus fatigue life curve (black) obtained from the superposition of the elastic (green) and plastic strain (orange) amplitude versus life curves; b) cycle to failure versus different microstructures of the as cast IN713C; c) plastic strain amplitude versus fatigue life data with the Coffin-Manson model calculation for each temperature; d) stress amplitude versus fatigue life data with the Basquin model calculation for each temperature.

Figure 5: Schematic of the produced bars (a), with their dimensions in mm, and depicting from where the sections to study the original microstructure have been taken. Micrographs of the sections studied for each microstructure (b), after being etched with Kalling's No. 2, showing the different grain size and shape between equiaxed, transition and columnar microstructures.

Figure 6: EBSD maps from sections of the as cast material with equiaxed (a), transition (b) and columnar (c) microstructure, showing the grain orientations from the Inverse Pole Figures (IPF) parallel to the casting direction, Z axis.

Figure 7: Micrographs of the radial section of a sample with equiaxed microstructure (a) and a detail of the dendritic structures within the grains under polarised light of the indicated area in (a).

Figure 8: Micrographs of the fracture surfaces of samples ERT06 (a) and EHT04 (b), showing the large presence of dendrites, indicated by red dashed lines, and the preferential oxidation during tests at HT. High magnification micrographs of the fracture surface of sample CHT05 (c and d) showing the dendritic structures and the major dendritic arm directions.

Figure 9: SEM images showing the extent of the dendritic arm line on the fracture surface of samples ERT06 (a), CRT06 (b) and EHT04 (c). High magnification SEM images of samples ERT06 (d) and CRT06 (e) showing the primary and secondary dendritic arms and the square shapes created with their intersection, with red arrows indicating dendrite-related secondary cracks and voids.

Figure 10: Micrographs of the cross section of three specimens after etching: EHT06 (a), THT03 (b) and CRT06 (c), showing their microstructure and crack initiation site indicated by red arrows.

Figure 11: SEM (secondary electron) image of the cross section of specimen ERT03 after being etched, with the areas where the EDS point analyses from Table 4 were obtained (a), SEM (backscatter electron) image of the same area without etching (b), layered EDS map image (c) with the separate EDS map for Ni (d), Al (e), Cr (f), Ti (g), Nb (h) and Mo (i), showing the element segregation.

Figure 12: SEM image of the cross section of specimen THT03 (a), layered EDS map image (b) with the separate EDS map for C (c), Ni (d), Al (e), Cr (f), Ti (g), Nb (h) and Mo (i) with the dendritic profile superimposed showing the element partitioning.

Figure 13: SEM images of the cross section of specimen CRT05, (b) is magnified area in (a) as indicated by a red dashed square, showing the changes induced in the crack propagation due to the presence of carbides.

Figure 14: EBSD maps of the cross sections of three fatigue specimens, EHT06 (a and d), THT03 (b and e) and CRT06 (c and f), with the crack initiation site indicated by red arrows and showing its grain orientation from the IPF parallel to the loading direction (a-c) and their Schmid Factor for the slip system {111}[110] parallel to the loading direction (d-f).

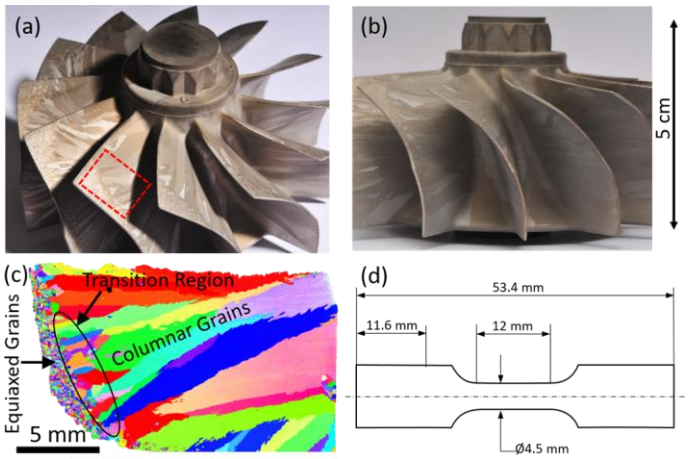

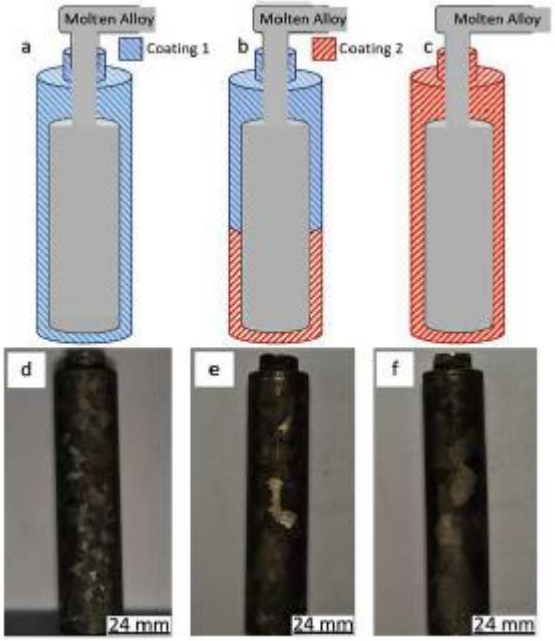

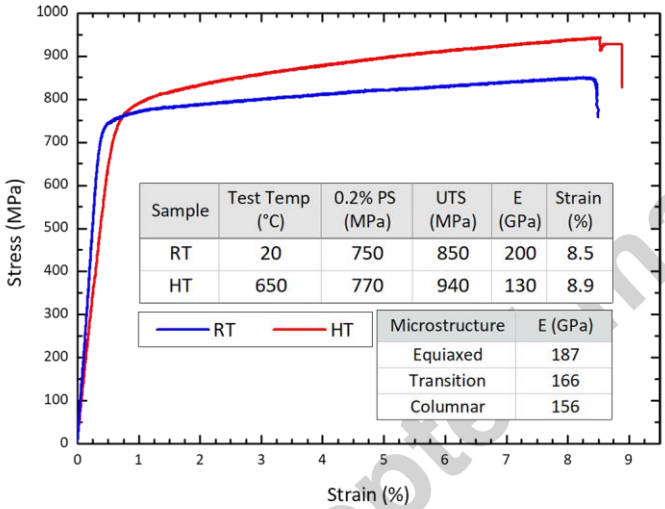

Sample	Test Temp (°C)	0.2% PS (MPa)	UTS (MPa)	E (GPa)	Strain (%)
RT	20	750	850	200	8.5
HT	650	770	940	130	8.9

Microstructure	E (GPa)
Equiaxed	187
Transition	166
Columnar	156

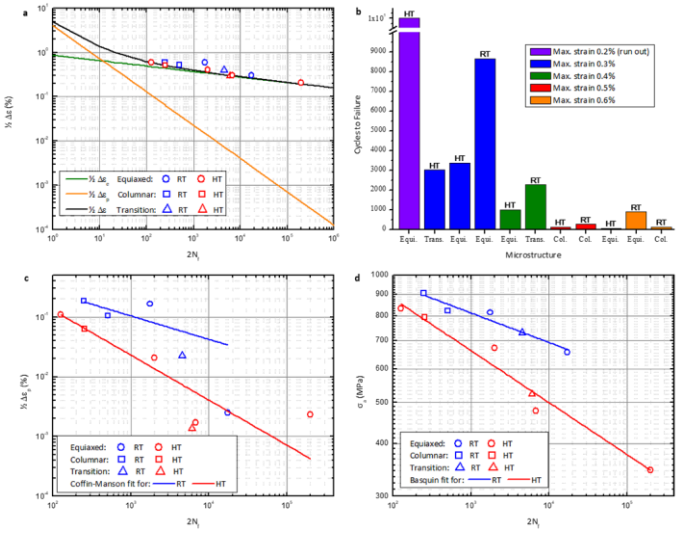

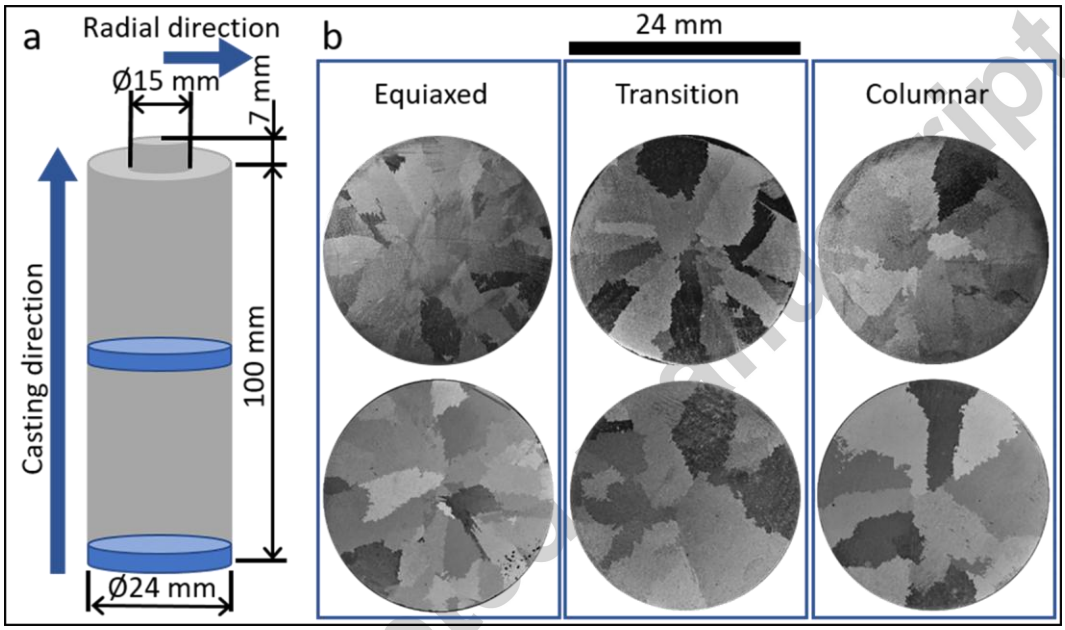

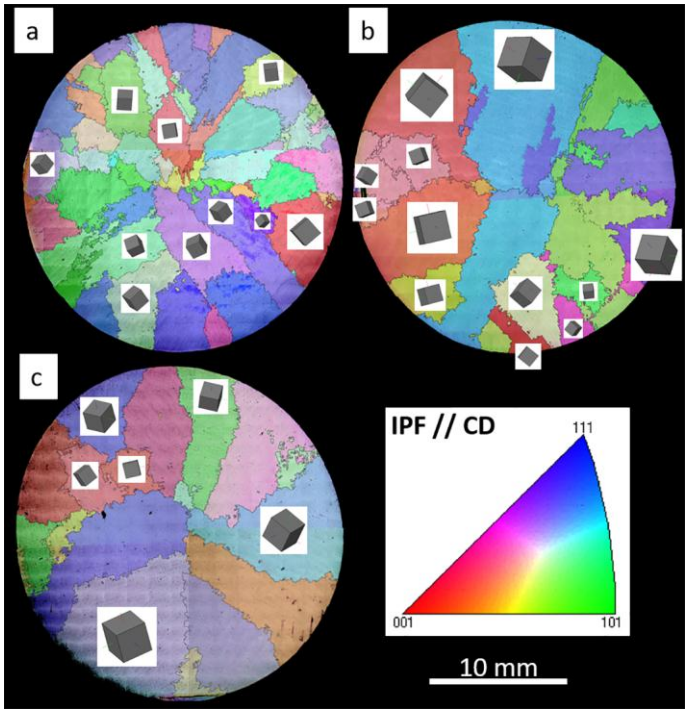

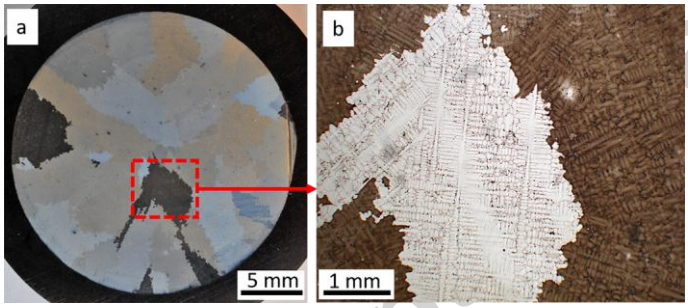

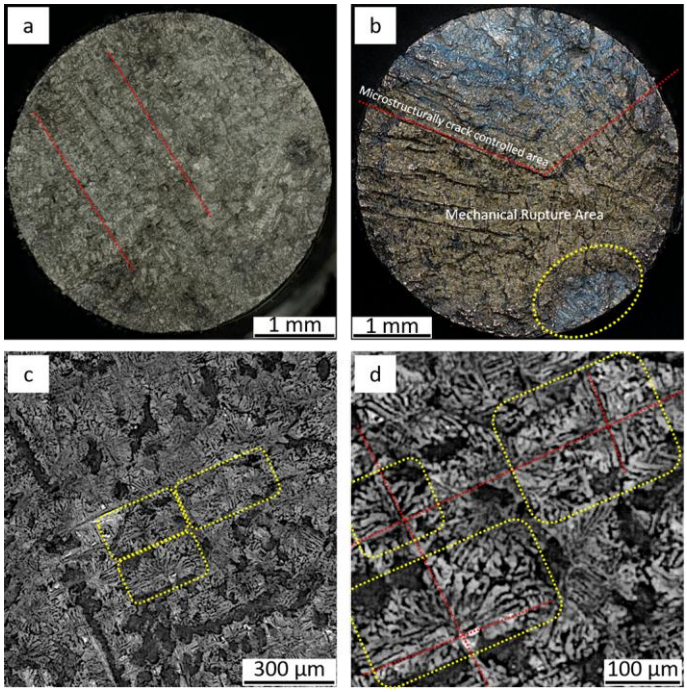

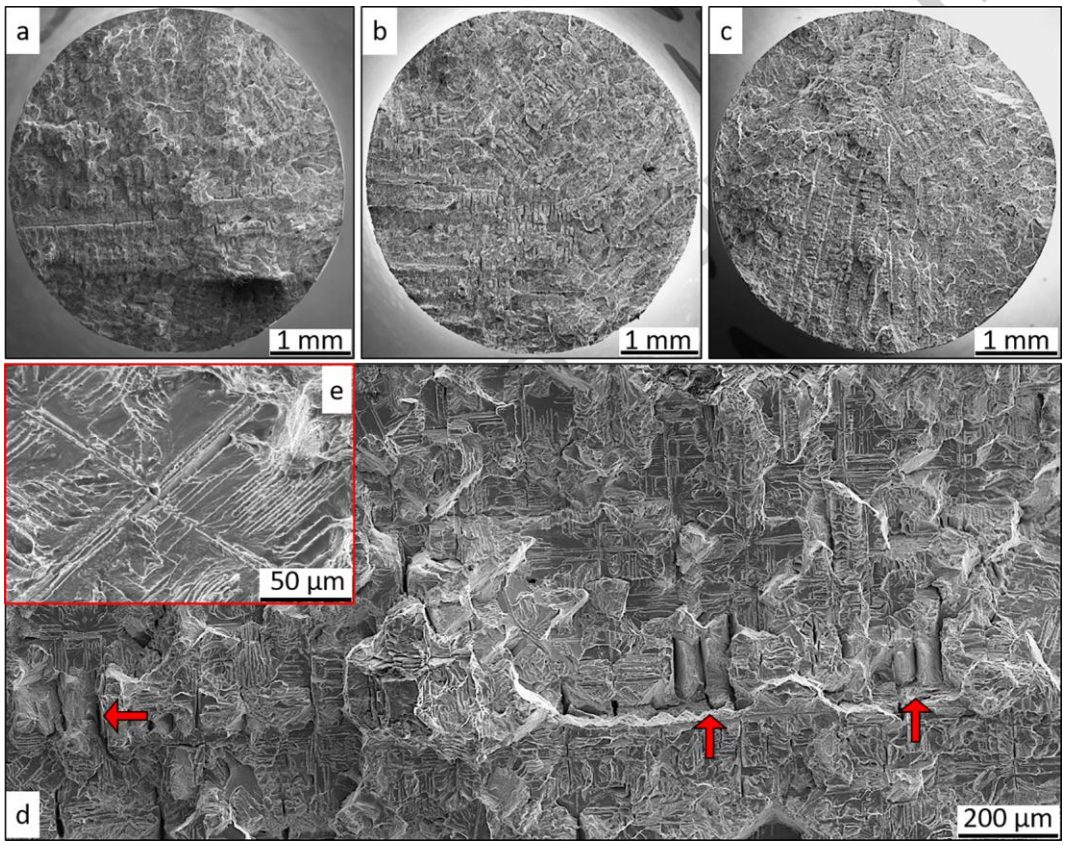

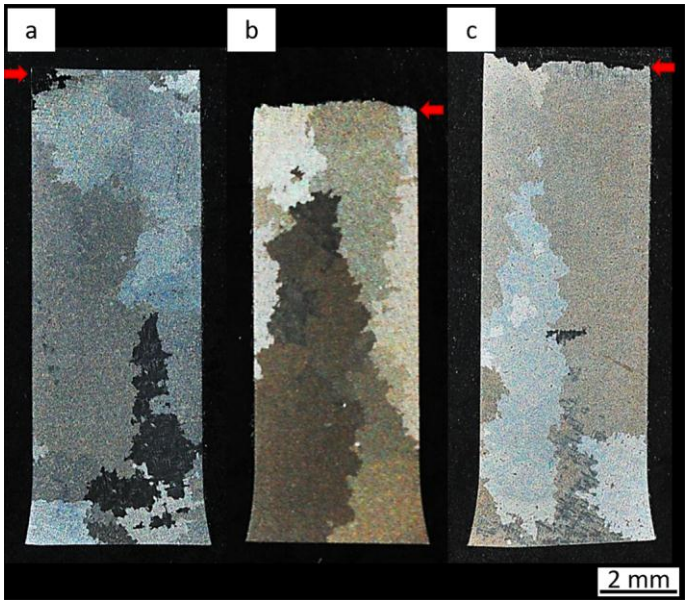

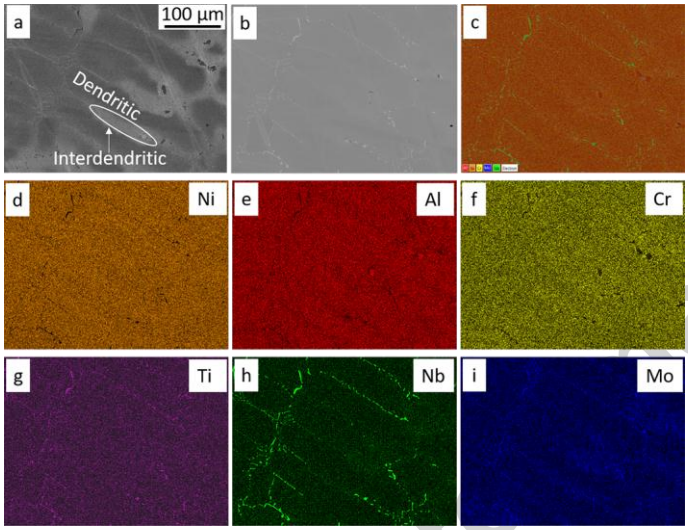

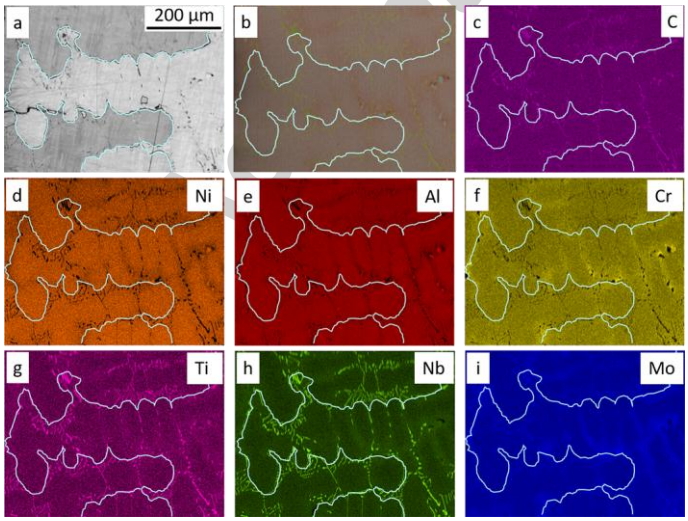

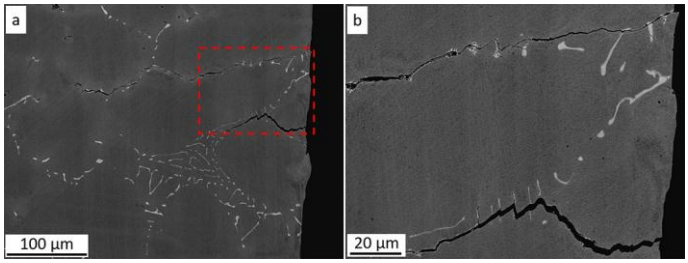

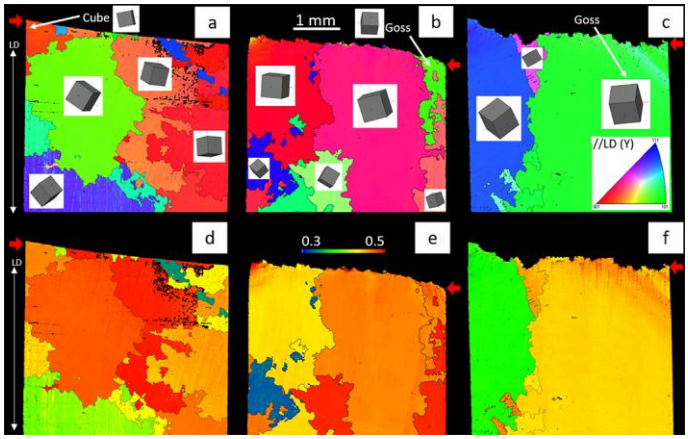

Highlights

- Fatigue analysis of three different microstructures representing the different microstructure present in real components.
- Presence of dendrites leading to differentiate element segregation areas and carbide precipitation in a patterned way.
- Carbides originating secondary cracks and altering the crack propagation path.
- Crack initiation preference on Cube and Goss grains, which have the same direction than the dendrite fast growth direction.